



Geophysical Research Letters

RESEARCH LETTER

10.1029/2018GL078156

Special Section:

Cassini's Final Year: Science Highlights and Discoveries

Key Points:

- Cassini observed three wave-like *ribbon* features in Saturn's 42N atmospheric jet from 2005 to 2014
- The ribbons' morphology, mean wavelengths, and propagation are consistent with Rossby waves
- Their propagation places constraints on atmospheric conditions within the jet

Supporting Information:

- Supporting Information S1
- Movie S1
- Movie S2
- Data Set S1
- Data Set S2

Correspondence to:

J. L. Gunnarson,
jacob.gunnarson@hamptonu.edu

Citation:

Gunnarson, J. L., Sayanagi, K. M., Blalock, J. J., Fletcher, L. N., Ingersoll, A., Dyudina, U. A., et al. (2018). Saturn's new ribbons: Cassini observations of planetary waves in Saturn's 42N atmospheric jet. *Geophysical Research Letters*, 45, 7399–7408. <https://doi.org/10.1029/2018GL078156>

Received 30 MAR 2018

Accepted 6 JUL 2018

Accepted article online 11 JUL 2018

Published online 8 AUG 2018

Saturn's New Ribbons: Cassini Observations of Planetary Waves in Saturn's 42N Atmospheric Jet

Jacob L. Gunnarson¹ , Kunio M. Sayanagi¹ , John J. Blalock¹ , Leigh N. Fletcher² , Andrew P. Ingersoll³ , Ulyana A. Dyudina³, Shawn P. Ewald³ , and Robert L. Draham^{1,4,5}

¹Department of Atmospheric and Planetary Sciences, Hampton University, Hampton, VA, USA, ²Department of Physics and Astronomy, University of Leicester, Leicester, UK, ³Division of Geological and Planetary Sciences, California Institute of Technology, Pasadena, CA, USA, ⁴Department of Physics, Juniata College, Huntingdon, PA, USA, ⁵The Institute of Optics, University of Rochester, Rochester, NY, USA

Abstract Using images from the Cassini spacecraft, we analyzed three *ribbon* waves in Saturn's 42°N eastward jet at 45°N, 42°N, and 39°N planetocentric latitudes. In this report, we demonstrate that the morphology, wavelength, and propagation of the ribbon waves are consistent with barotropic Rossby waves with a smaller baroclinic component. We report on the appearance and disappearance of these waves during Cassini's mission. We suggest that the temporal evolution of these waves are related to the great Saturn storm of 2010–2011.

Plain Language Summary During their 1980 and 1981 flybys of Saturn, the Voyager spacecraft imaged a dark, sinuous line encircling the planet. This feature, dubbed the *ribbon* wave after its visual appearance, was embedded in an atmospheric jet stream at 42N latitude. The Cassini spacecraft also discovered waves in the 42N jet during its 2004–2017 Saturn mission. Using images taken by Cassini, we have identified the ribbon waves as Rossby waves, that is, planet-scale waves that are common in atmospheres, including that of the Earth. Unlike Earth's atmospheric Rossby waves, which are only visible as undulations on weather maps, Saturn's ribbons are visually striking and may be some of the most prominent examples of Rossby waves in the Solar System. The ribbons are composed of a number of wavelengths, each of which is affected differently by the atmosphere and move at different speeds. By measuring the differing speed of these wavelength components, we compared the behavior of the ribbons to theoretical predictions for Rossby waves and estimated basic properties of the atmosphere. Because the ribbons likely extend deep into the atmosphere, they may help shed light on the how the atmosphere behaves at depths that Cassini was not able to observe directly.

1. Introduction

One of the prominent features of Saturn's atmosphere discovered by the Voyager spacecraft was a dark, sinuous line encircling the planet at 42°N latitude (we use planetocentric latitude throughout this report), which was dubbed the *ribbon* wave after its visual appearance (Smith et al., 1981, 1982). We use the term *ribbon* and *ribbon wave* throughout to refer to planet-encircling features that have north-south oscillations, visible as distinct divisions within, or boundaries between, cloud bands. This is a morphological classification, as features with a similar appearance (e.g., Jupiter's ribbon, Cosentino et al., 2015, and 20°S wave, Rogers et al., 2016) may have different dynamical origins, while some features with broadly similar dynamics (e.g., Jupiter's equatorial hot spots (Choi et al., 2013)) do not have ribbon-like morphologies.

Subsequent analysis of Voyager 2 images determined that the ribbon represented the meandering core of an eastward jet with a wind speed of about 150 m/s. The ribbon was also a boundary between a cyclonic zone to the north and an anticyclonic zone to the south. Because of its presence at a sharp meridional potential vorticity gradient and its north-south meandering, the ribbon was assumed to be a Rossby wave—a planetary-scale wave with the restoring force provided by a positive potential vorticity gradient.

Sromovsky et al. (1983) measured the change in the ribbon's Fourier phase spectrum over time and found a Rossby wave-like relation between the phase velocity and wavenumber of each Fourier component. However

the dispersion relation used to fit the data did not include the effects of the background wind profile or a finite Rossby deformation radius (see section 4.3).

Godfrey and Moore (1986) proposed that the ribbon wave was a manifestation of baroclinic instability in the jet. Sayanagi et al. (2010) used numerical simulations to show that baroclinic instability modes in the peak of the jet quickly grow and saturate nonlinearly, producing a long-lived wave with properties matching those observed for the ribbon.

Sánchez-Lavega (2002) observed Saturn's 42°N ribbon using Hubble Space Telescope images from 1994 to 1995. The ribbon's meridional peak-to-trough amplitude was close to the resolution limit of Hubble and thus its propagation could not be analyzed. This was the only observation of the ribbon between the Voyager and Cassini eras.

Here, we used images from the Cassini spacecraft during its entire Saturn mission from 2004–2017 to study ribbon waves in the 42°N jet. We report that three distinct waves at 45°N, 42°N, and 39°N (hereafter referred to as the *north*, *mid*, and *south* ribbons) appeared and disappeared over the course of a 9-year period from 2005 to 2014. In this report, we demonstrate that the morphology, wavelength, and propagation of Saturn's ribbon waves are consistent with Rossby waves that are primarily barotropic with a smaller baroclinic component.

2. Cassini ISS Images

We used images from the wide-angle camera (WAC) and narrow-angle camera (NAC) of Cassini's Imaging Science Subsystem (ISS; Porco et al. (2004)) for our analysis. Images were processed using the USGS ISIS 3 software package *cisscal* (Anderson et al., 2004; Gaddis et al., 1997; Keszthelyi et al., 2013) which uses the geometric model and the photometric calibration derived from Cassini ISS CALibration software v3.6, as described in Porco et al. (2004) and West et al. (2010). Image navigation procedures used equatorial and polar radii of 60,268 and 54,364 km, respectively (Lindal et al., 1985). All images were map projected to a latitude-longitude cylindrical projection at 0.1°/pixel resolution for wide-angle camera images and 0.01°/pixel resolution for narrow-angle camera images. We use System III longitude (Archinal et al., 2011; Seidelmann et al., 2007) throughout this report.

Several filters were useful for our analysis (see Roman et al., 2013). The MT3 (889 nm) methane absorption filter shows variation in tropospheric haze around 100 mbar, while the MT2 (727 nm) filter sounds deeper into the haze. The CB2 (750 nm) methane continuum filter penetrates deeper into the atmosphere and shows thick ammonia cloud tops at around 1–2 bars.

3. Methods

3.1. Ribbon Tracing

The ribbons were visible as sharp boundaries between bright and dark areas in CB2 images. We manually selected points at ~ 0.5 – 1.0° longitude intervals (significantly smaller than the distance between crests and troughs) along these boundaries, which yields the latitude of the waves as a function of longitude. The points were logged with ISIS 3's *tracking* tool. These sets of latitude-longitude points are hereafter referred to as *traces*. We examined images over the entire Cassini image data set for our analysis and made 251 traces. The list of images and the traces are available as Data Sets S1 and S2, respectively, in the supporting information.

3.2. Spectral Analysis

An obvious method for analyzing the ribbon traces is the discrete Fourier transform because it allows each wavenumber component to be separately evaluated for amplitude and phase. However, a single high-resolution image of Saturn at 42°N covers at most about 120° in longitude because the apparent size of Saturn is larger than the camera's field of view. As a result, the Fourier transform must be taken over an incomplete longitudinal range and will have correspondingly incomplete wavenumber coverage. There are two possible methods to compensate for an incomplete longitudinal coverage: apodizing the trace (i.e., setting the trace equal to the average latitude of the ribbon outside the covered longitude range, as in Sromovsky et al., 1983) and using a 360° mosaic made over one Saturn rotation to trace the ribbon.

We initially attempted to use both methods in our analysis to compensate from the incomplete longitude coverage, but each has significant drawbacks. Apodizing the trace greatly decreases the resolution of the amplitude spectrum and corrupts the phase spectrum, leading to spurious results for dispersion analysis. Tracing a 360° mosaic results in an acceptable amplitude spectrum, but dispersion cannot be reliably

calculated as the propagation speed of each wavenumber component is different and a mosaic that combines multiple images captured over a 10-hr planetary rotation cannot be made to account for this dispersion.

For these reasons, we took the approach of Godfrey and Moore (1986) by measuring the distance between the peaks and troughs of the wave using traces of single images. Each trace was interpolated onto a regular grid using a cubic spline, smoothed by a moving average filter with a 1.5° wide window ($\sim 1,000$ km at 42° N) and then the longitude of the wave's peaks and troughs was identified with a peak-finding algorithm. The smoothing window size was chosen because it minimized the number of short wavelength, small amplitude peaks/troughs (primarily interpolation artifacts) while preserving the dominant wavelengths, which were much longer than the smoothing window. The latitude for each peak and trough was taken from the unsmoothed trace to avoid the diminishing amplitude effects of smoothing. This process is illustrated in supporting information Figures S2 and S3.

Compared to the Fourier transform, measuring the distance between the peaks and troughs is a more intuitive way to interpret the ribbons' characteristic length scales, and it is not affected by an incomplete longitude range. From these data, peak-to-peak wavelength, meridional amplitude, and the mean latitude of the wave can be extracted. One disadvantage of this method is that it is biased toward high wavenumber modes. Low wavenumber modes (i.e., modes with wavelengths significantly longer than the most common wavelength) are present as undulations in the latitude of the peaks/troughs themselves but not as peaks/troughs that are detected by our algorithm.

3.3. Dispersion Measurement

As previously discussed, the Fourier transform is problematic for analyzing the ribbon waves, but it can be carefully applied to yield the phase velocity of each wavenumber component and thus the dispersion of the waves.

We selected pairs of traces made from images covering the same longitude range and separated in time by about one Saturn rotation. The pairs were shifted in longitude to account for the background eastward zonal wind (54.8 m/s at 44.6° N in 2008 from Blalock et al. (2016); see supporting information Figure S1) to minimize phase ambiguity at higher wavenumbers. They were then trimmed to cover the same longitudinal domain, which is necessary for directly comparing their Fourier spectra. We computed phase velocity using the following equation

$$c(n_x) = \frac{a}{n_x \Delta t} \Delta \varphi(n_x) \quad (1)$$

where $c(n_x)$ is the zonal phase velocity, a function of the planetary zonal wavenumber n_x (i.e., the number of wave cycles around 360° longitude), a is the distance to Saturn's axis of rotation at the mean latitude of the wave, Δt is the time separation between the traces/images, and $\Delta \varphi(n_x)$ is the difference in phase for each Fourier component in the two traces.

We were only able to perform this analysis for the north ribbon using 16 images captured by Cassini between February and May 2008. Due to a lack of suitable high-resolution image pairs, we were not able to perform this analysis on the mid and south ribbons.

To fit a dispersion relation to the data, we only used data with wavenumbers that corresponded to spectral peaks. We found that the minimum amplitude of the peaks in the north ribbon's Fourier spectrum was about 0.025° ; therefore, we only considered phase velocities that had at least this Fourier amplitude (see supporting information Figure S4). The phase velocity measurements corresponding to spectral peaks were then binned by wavenumber with a bin size of 5, chosen so that most bins had about 5 or more points. Each bin was represented with a single point located at the center of the bin and the mean phase velocity of all data in the bin, with an uncertainty calculated by taking the standard deviation of phase velocities within the bin. We fit the dispersion relation to these points using a least squares fit (Markwardt, 2009). Phase velocities that did not correspond to spectral peaks were not binned and fitted.

Because our traces cover an incomplete longitudinal range, the phase velocity cannot be calculated for every single wavenumber. However, having a measurement for each wavenumber is not essential to determine the dispersion of the waves.

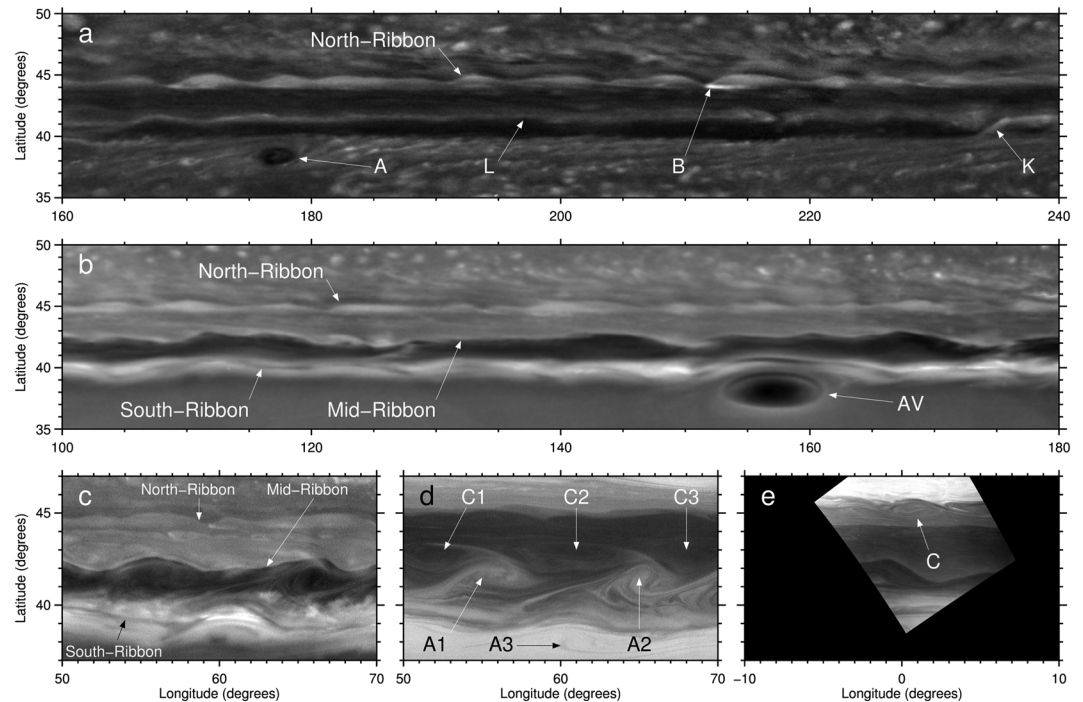


Figure 1. Morphology of the 42°N jet as seen by Cassini ISS. (a) WAC CB2 mosaic, 13 January 2008. (b) WAC CB2 mosaic, 10 December 2012. (c) NAC CB2 image, 20 January 2012. (d) NAC MT2 image, simultaneous with (c). (e) NAC MT2 image, 5 May 2013. ISS = Imaging Science Subsystem; WAC = wide-angle camera; NAC = narrow-angle camera.

4. Results and Discussion

4.1. Morphology Changes

Cassini found that the 42°N jet's appearance had dramatically changed since the Voyager and Hubble observations. When the spacecraft entered orbit around Saturn in July 2004, the jet was still mostly in the darkness of northern winter and in the ring shadow. When the jet became visible to Cassini in October 2005, a ribbon wave had formed on the northern flank of the jet (see below) and the Voyager era ribbon at the peak of the jet had disappeared. In place of the Voyager-era ribbon was a thin bright line (*L* in Figure 1a) with abrupt southward kinks about every 90–180° in longitude (e.g., *K* in Figure 1a). Cassini observed similar morphology in the southern hemisphere jets at 42°S and 55°S, which also host transient wave activity (Sánchez-Lavega et al., 2000; Vasavada et al., 2006). Cassini's Visual and Infrared Mapping Spectrometer (VIMS) observed this line at 42°N as a band of thick clouds backlit against the 5- μ m glow of the planet's interior (Figure 3 in Choi et al. (2009); this line is misidentified as the ribbon in earlier literature; e.g., Del Genio et al., 2009). At some longitudes, low-amplitude wave-like morphology was visible, but there was no well-defined wave at the peak of the jet from 2005 to 2010.

When first imaged by Cassini in October 2005, the north ribbon was at the northern flank of the jet at 44°N (Figure 1a). The southern (northern) side of the wave was bright (dark) in CB2 and dark (bright) in MT3. VIMS mosaics hint at the north ribbon as a wavy boundary between a cloud-free area to the south and an area of thick clouds to the north (Choi et al., 2009). On several occasions NAC MT3 and MT2 images revealed spiraling cloud patterns with cyclonic vorticity nestled in the peaks of the wave (e.g., *C* in Figure 1e). Small bright clouds were frequently observed being sheared from the troughs of the north ribbon (e.g., *B* in Figure 1a).

The north ribbon underwent significant changes in its mean latitude (see Figure 2). From October 2005 to September 2010 its mean latitude increased from 44.2°N to 45.7°N. In December 2010, a violent convective storm—the *Great White Spot* or *2010–2011 storm*—erupted between 32°N and 38°N latitudes, eventually engulfing the southern flank of the 42°N jet. Between September 2010 and February 2011, the north ribbon moved south to 44.5° and decreased in amplitude, indicating that the storm had some effect on the wave.

In June 2011, the storm activity quickly abated after the head of the storm and a large anticyclonic vortex collided (Sayanagi et al., 2013). Around this time, the mid and south ribbons began to appear at 39°N and

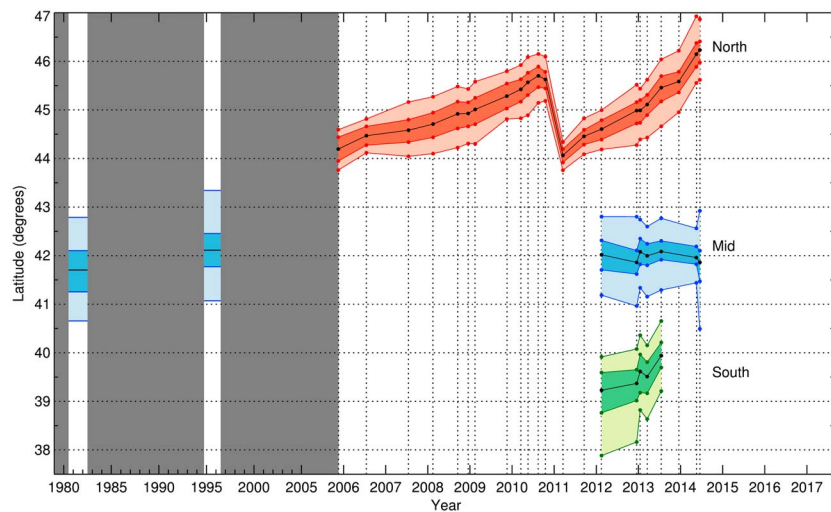


Figure 2. Latitude of the ribbon waves over time. The black lines indicate the mean latitude, the darker shaded areas indicate the mean latitudes of the peaks and troughs, and the lighter shaded areas indicate the maximum latitude of the peaks and troughs. Dark grey areas indicate no available data. Each vertical dotted line represents a measurement (binned by month). The 1981 and 1995–1996 data were taken from Sromovsky et al. (1983) and Sánchez-Lavega (2002), respectively.

42°N latitudes, respectively (annotated in Figures 1b and 1c). The south ribbon seems to have formed from the turbulent northern boundary of the storm's wake, while the mid ribbon gradually evolved from turbulent features at the peak of the jet.

The mid ribbon was visible in CB2 as a sharp boundary between a bright band to the north and a dark band to the south at the same latitude as the Voyager era ribbon. High-resolution MT2 and CB2 movies (supporting information movies S1 and S2) showed cyclonic eddies embedded in the troughs and anticyclonic spirals in the peaks. Figure 1d shows the embedded bright anticyclonic eddies (A1 and A2) and dark cyclonic eddies (C1, C2, and C3).

The south ribbon was prominent in MT2 as a wavy boundary at 39°N, on the southern flank of the jet, with anticyclones embedded in the peaks (A3 in Figure 1d). The large anticyclonic vortex formed during the 2010–2011 storm (AV in Figure 1b) interacted with the wave, thus potentially disturbing the nearby mid ribbon as well. (This is not the same anticyclone as the one annotated A in Figure 1a.)

Both the north and south ribbons drifted poleward between 2011 and 2014, with the north ribbon migrating over 2° north (Figure 2). The mid ribbon remained at the peak of the jet. The south ribbon diminished in amplitude and its wavy morphology ceased in late 2013. The now straight boundary between the bright band to the south and the dark band to the north remained. The north and mid ribbons disappeared in mid-2014. The dark line of the mid ribbon remained but with only occasional wave-like morphology at some longitudes, much as it had appeared early in Cassini's mission. By the end of the Cassini mission in 2017, there were no ribbon waves in the jet.

The ribbons appeared as meandering paths embedded in vortex streets, similar to barotropic instabilities produced in numerical simulations (see Figures 13 and 15 in Flierl et al., 1987, and Figures 4 and 5 in Poulin & Flierl, 2003) and laboratory experiments (Barbosa Aguiar et al., 2010). Simulations of Saturn's north polar hexagon (Morales-Juberias et al., 2015) suggest that vortex street morphology arises in barotropic conditions, while a meandering morphology occurs in baroclinic conditions. As the ribbons' appearance is somewhere in between these two extremes, we conclude that a mix of barotropic and baroclinic conditions is likely at play in the 42°N jet.

While a radiative transfer analysis is beyond the scope of this study, we can infer the vertical extent of these waves by comparing their appearance at different wavelengths (Roman et al., 2013). All three waves were seen in the MT3 and CB2 filters; therefore, they extended from ~100 mbar down to at least 1 bar, corresponding to a vertical extent in excess of ~100 km. There was no detectable east-west phase shift or decrease in meridional extent between simultaneous MT3 and CB2 images, which points to the ribbons being primarily barotropic, at least in the altitude range sounded by these filters.

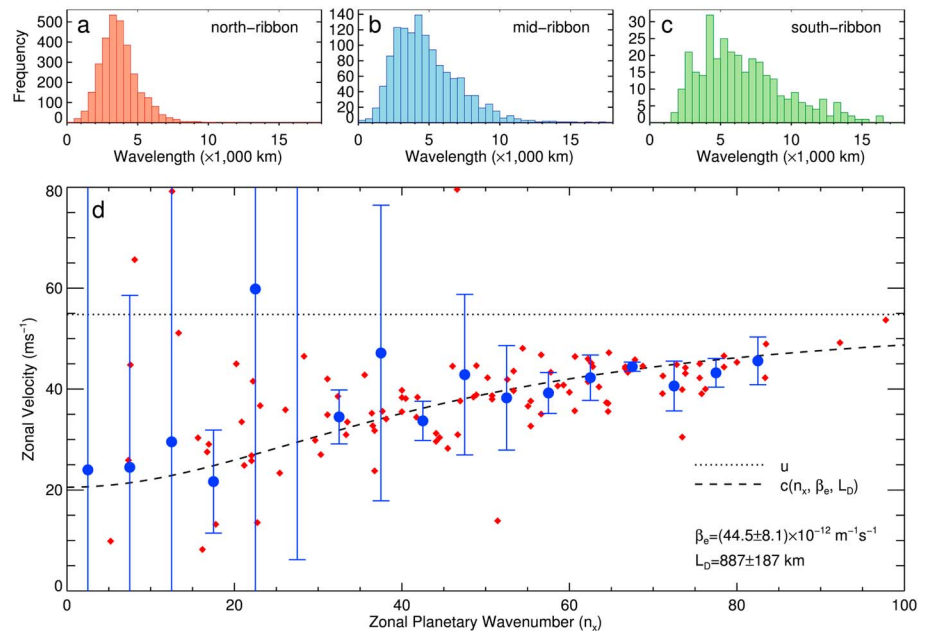


Figure 3. Observed properties of the ribbon waves. (a–c) Histograms of the ribbons’ peak-to-peak wavelengths. (d) Dispersion of the north ribbon. Red diamonds are phase velocities that correspond to spectral peaks, which have been binned into the blue dots and error bars (see section 3.3). The blue dots are fitted with a dispersion relation (dashed line; see equation (6)).

The ribbon waves were also visible in 5 μm images captured by VIMS. The level of features sensed by the 5 μm images is between 1 and 4 bar, probably corresponding to the base of the clouds sensed by the CB2 filter (Choi et al., 2009). In high resolution 5-μm mosaics taken in 2012, the mid ribbon is visible as a sharp dark line while the south ribbon is conspicuous as a boundary between an area of thick clouds to the north and the cloud-free wake of the 2010–2011 storm (Figures 2 and 3 in Sromovsky et al., 2016). From these observations we conclude that the ribbons extended from the high tropospheric hazes to the ammonia cloud deck and possibly deeper.

It has been previously reported that Cassini’s Composite Infrared Spectrometer may have detected thermal signatures of the mid ribbon (Figure 6.23 in Del Genio et al., 2009). Periodic temperature anomalies were detected at 42°N by Cassini’s Composite Infrared Spectrometer; however, these anomalies were likely due to poorly calibrated pixels. For subsequent calibrations, no periodic temperature anomalies are evident.

4.2. Wavelength Spectra

Our peak-to-peak zonal wavelength measurements are shown in Figures 3a–3c. The peak wavelength was 3,000–3,500 km for the north ribbon and 4,000–4,500 km for the mid and south ribbons. The wavelength distribution for the north ribbon appears almost Gaussian, with almost all wavelengths concentrated between 1,000 and 7,000 km. The distributions for the mid and south ribbons have a higher number of long-wavelength components, which corresponds well to their visual appearances.

The mid ribbon’s peak wavelength is similar to what has been previously reported for the Voyager and Hubble observations—Godfrey and Moore (1986) and Sánchez-Lavega (2002) obtained 5,710 and 4,200 km, respectively. Sánchez-Lavega et al. (2012) measured the wavelength of the disturbances on the northern boundary of 2010–2011 storm’s wake and obtained wavelengths between 4,500 and 11,000 km, with a peak of 4,800 km, further suggesting that the south ribbon evolved from the storm’s wake.

As Rossby waves owe their existence to planetary rotation, they should have wavelengths longer than the Rossby deformation radius (L_D), the horizontal length scale beyond which the Coriolis force dominates over buoyancy forces.

$$L_D = \frac{N_B D}{f_0} \quad (2)$$

where N_b is the Brunt-Väisälä frequency, D is a characteristic vertical length scale, and f_0 is the Coriolis parameter. For the north ribbon, we found $L_D = 889 \pm 187$ km by dispersion analysis (see section 4.3), and Read et al. (2009) obtained $L_D \approx 2,000$ km in the 42°N jet using Arno'ld's Second Criterion, both of which are shorter than the ribbons' peak wavelengths. Therefore, we conclude that the ribbons' wavelengths are consistent with Rossby waves.

4.3. Wave Propagation and Dispersion

The result of our dispersion analysis of the north ribbon in early 2008 is shown in Figure 3d. While there is substantial scatter, there is a clear trend to slower zonal phase speeds (westward propagation relative to the background wind) at lower wavenumbers, which is characteristic of Rossby waves.

To put our measurements in an analytic perspective (following Pedlosky, 2003), consider a Rossby wave mode propagating purely zonally in a single layer of depth D , which can be modeled with the stream function

$$\psi = Ae^{i(kx - \omega t)} \quad (3)$$

where A is the amplitude, ω is the frequency, and k is the zonal wavenumber, defined as $k = 2\pi/L_x$, where L_x is the zonal wavelength ($k = n_x/a$). Models of Rossby wave stream functions typically include meridional and vertical wavenumbers, as well as a depth-dependent amplitude (e.g., Sánchez-Lavega et al., 2014). While it is clear from Figure 2 that the north ribbon propagated meridionally on the time scale of years, between 2006 and 2010 its poleward velocity was about $0.4^\circ/\text{year}$ or 0.003 m/s. This is several orders of magnitude smaller than the north ribbon's zonal phase speeds in Figure 3d, and therefore, the meridional wavenumber can be neglected in this analysis. We can also neglect any vertical dependence because we do not see any significant change in meridional extent or phase with depth.

If we make the approximation that N_b does not vary much with depth in the wave propagation layer (for analytic expedience; see Sánchez-Lavega, 2011), we can write the linearized conservation of potential vorticity as

$$\left(\frac{\partial}{\partial t} + u \frac{\partial}{\partial x} \right) \left[\nabla^2 \psi - \frac{1}{L_D^2} \psi \right] + \beta_e \frac{\partial \psi}{\partial x} = 0 \quad (4)$$

where β_e is the potential vorticity gradient, defined as

$$\beta_e = \beta + \beta_y + \beta_z \quad (5)$$

where β is the planetary vorticity gradient, β_y is the zonal wind curvature, and β_z is the vertical wind curvature (Fletcher et al., 2016; Read et al., 2009). To provide a restoring force which allows Rossby waves to propagate, β_e must be positive. Substituting equation (3) into equation (4), we obtain the following dispersion relation

$$c = u - \frac{\beta_e}{k^2 + 1/L_D^2} \quad (6)$$

where c is the wave's zonal phase speed. Because β_e must be positive, c is always less than u (i.e., westward propagation relative to u).

We fit our dispersion measurements to equation (6), setting $u = 54.8$ m/s (Blalock et al., 2016), but letting β_e and L_D vary freely. The best fit was achieved with $\beta_e = (44.5 \pm 8.1) \times 10^{-12} \text{ m}^{-1} \text{ s}^{-1}$ and $L_D = 887 \pm 187$ km (see Figure 3) with $\chi^2 = 4.10$. u has a standard deviation of 12.2 m/s (Blalock et al., 2016). As a significant number of the phase velocities at higher wavenumbers in Figure 3d are at or above the lower bound of u (42.6 m/s) and stable Rossby waves cannot be stationary or propagate eastward with respect to the wind, we can dismiss the lower bound of u . Fitting using the upper bound of u (67.0 m/s) yielded $\beta_e = (150 \pm 32) \times 10^{-12} \text{ m}^{-1} \text{ s}^{-1}$ and $L_D = 520 \pm 91$ km with $\chi^2 = 4.97$. For the remainder of the report, we will use the fit derived from the mean wind speed of 54.8 m/s.

If we assume that $N_b \approx 1.7 \times 10^{-3} \text{ s}^{-1}$ in the ammonia cloud (Sánchez-Lavega et al., 2012), using equation (2) yields $D \approx 125 \pm 26$ km. If the top of the north ribbon propagation layer is at 100 mbar, then the bottom is between 600 mbar and 1.5 bar, although it is likely closer to the latter because the ribbons are present at the ammonia cloud top around 1–2 bars.

Comparing the peak wavelength and Rossby deformation radius may help to distinguish between barotropic and baroclinic Rossby waves. The ratio of kinetic energy to potential energy of a Rossby wave, averaged over one period, can be written as

$$\frac{\langle KE \rangle}{\langle PE \rangle} = 4\pi^2 \frac{L_D^2}{L_x^2} \quad (7)$$

(Pedlosky, 2003). If this ratio is much more than unity (e.g., if L_D is very large), the wave is barotropic, and if the ratio is much less than unity, the wave is baroclinic. For the north ribbon ($L_x \approx 3,250$ km and $L_D = 889$ km), $\langle KE \rangle / \langle PE \rangle \approx 3$, which indicates that it is primarily, but not purely, barotropic. If we use the same L_D for the mid and south ribbons, $\langle KE \rangle / \langle PE \rangle \approx 1.7$, which is still mostly barotropic but with a larger baroclinic component. If we use $L_D \approx 2,000$ km (Read et al., 2009), this ratio is larger and more suggestive of pure barotropic Rossby waves: ~ 15 for the north ribbon and ~ 9 for the mid and south ribbons.

While we could not perform dispersion analysis on the mid and south ribbons, they too likely exhibit Rossby wave-like propagation. Sromovsky et al. (1983) found that the Voyager era ribbon, which was at the same latitude as the Cassini era mid ribbon, propagated westward relative to the zonal wind. Sánchez-Lavega et al. (2012) found that the wave-like northern boundary of the 2010–2011 storm, which would emerge months later as the south-ribbon, also moved westward relative to the zonal wind. This was likely not due to a decrease in the background wind as Sayanagi et al. (2013) determined that the zonal wind actually increased at that latitude, presumably because of the latent heat released by the storm and the resulting thermal wind.

5. Conclusions

The study of planetary-scale Rossby waves, such as Saturn's ribbons and hexagon, and Jupiter's equatorial hot spots, is important to our understanding of the large-scale atmospheric dynamics of gas giant planets. We have determined that the ribbon waves in Saturn's 42°N jet are likely Rossby waves based on the following observations

1. *Morphology.* The ribbons have a striking visual similarity to Rossby waves and simulations of nonlinear unstable jets. Their appearance as meandering lines embedded in vortex streets suggests that they are primarily barotropic but with some baroclinic component.
2. *Wavelength spectra.* All three ribbons have peak wavelengths longer than the Rossby deformation radius, which is expected for Rossby waves.
3. *Propagation.* The north ribbon's phase velocities are well fit by a simple Rossby wave dispersion relation with a finite Rossby deformation radius. Comparing the peak wavelengths of the ribbons to this deformation radius suggests that they are primarily barotropic Rossby waves with a smaller baroclinic component. Sromovsky et al. (1983) and Sánchez-Lavega et al. (2012) give evidence that the mid and south ribbons propagate westward relative to the background wind, which is characteristic of Rossby waves.

The zonal propagation of the ribbon waves places constraints on the atmospheric conditions in the 42°N jet. The potential vorticity gradient in the jet must have been positive in order for the ribbons to propagate. For the north ribbon, we obtained $\beta_e = (44.5 \pm 8.1) \times 10^{-12} \text{ m}^{-1} \text{ s}^{-1}$, which is about 10 times the planetary vorticity gradient ($\beta = 4 \times 10^{-12} \text{ m}^{-1} \text{ s}^{-1}$). We also obtained a Rossby deformation radius of 887 ± 187 km.

While the ribbons are discrete and almost certainly nonlinear waves, our analysis is based on a linear plane wave approximation. We have made further simplifications in the vertical structure of the waves and atmosphere in our model stream function because of a lack of observed vertical variation in the waves and for analytic simplicity. However, we obtained a good fit to our derived Rossby wave dispersion relation with reasonable values for β_e and L_D .

Questions about the ribbons still remain: What causes them to rapidly appear and disappear? What is their vertical structure? Do multiple ribbons interact with each other? Further stability analysis and numerical modeling of the 42°N jet may provide more insight into the atmospheric conditions required to produce these waves. Radiative transfer modeling using high-resolution Cassini ISS and VIMS data may shed more light on the vertical structure of the ribbons. Hopefully future spacecraft missions to Saturn will probe deeper into the atmosphere to reveal the waves and atmospheric conditions at and below the ammonia cloud layer.

Acknowledgments

Our data are available in the supporting information. We used Cassini ISS images available from the Planetary Data System (PDS). We also acknowledge use of the GNU parallel software (Tange, 2011) for processing images used in this study. We thank R. G. Cosentino and an anonymous reviewer for their comments, which greatly strengthened this report. This work was supported by NASA Cassini Data Analysis Program grant NNX15AD3392 to K. M. S. L. N. F. was supported by a Royal Society Research Fellowship and European Research Council Consolidator Grant (under the European Union's Horizon 2020 research and innovation program, grant agreement 723890) at the University of Leicester.

References

- Anderson, J. A., Sides, S. C., Soltesz, D. L., Sucharski, T. L., & Becker, K. J. (2004). Modernization of the integrated software for imagers and spectrometers. In *Paper Presented at 35th Lunar and Planetary Science Conference*. League City, TX. Retrieved from <http://adsabs.harvard.edu/abs/2004LPI....35.2039A>
- Archinal, B. A., A'Hearn, M. F., Bowell, E., Conrad, A., Consolmagno, G. J., Courtin, R., et al. (2011). Report of the IAU working group on cartographic coordinates and rotational elements: 2009. *Celestial Mechanics and Dynamical Astronomy*, *109*(2), 101–135. <https://doi.org/10.1007/s10569-010-9320-4>
- Barbosa Aguiar, A. C., Read, P. L., Wordsworth, R. D., Salter, T., & Yamazaki, Y. H. (2010). A laboratory model of Saturn's North Polar Hexagon. *Icarus*, *206*(2), 755–763. <https://doi.org/10.1016/j.icarus.2009.10.022>
- Blalock, J. J., Sayanagi, K. M., Ingersoll, A. P., Dyudina, U. A., & Ewald, S. P. (2016). Measurements of seasonal changes in Saturn's zonal wind and vertical wind shear between 2004 and 2016 from Cassini ISS images. In *Paper presented at 48th meeting of the American Astronomical Society Division for Planetary Sciences* (p. 514). Pasadena, CA. Retrieved from <http://adsabs.harvard.edu/abs/2016DPS....4851409B>
- Choi, D. S., Showman, A. P., & Brown, R. H. (2009). Cloud features and zonal wind measurements of Saturn's atmosphere as observed by cassini/VIMS. *Journal of Geophysical Research*, *114*, E04007. <https://doi.org/10.1029/2008JE003254>
- Choi, D. S., Showman, A. P., Vasavada, A. R., & Simon-Miller, A. A. (2013). Meteorology of Jupiter's equatorial hot spots and plumes from Cassini. *Icarus*, *223*(2), 832–843. <https://doi.org/10.1016/j.icarus.2013.02.001>
- Cosentino, R. G., Simon, A., Morales-Juberías, R., & Sayanagi, K. M. (2015). Observations and numerical modeling of the Jovian Ribbon. *The Astrophysical Journal Letters*, *810*(1), L10. <https://doi.org/10.1088/2041-8205/810/1/L10>
- Del Genio, A. D., Achterberg, R. K., Baines, K. H., Flasar, F. M., Read, P. L., Sánchez-Lavega, A., & Showman, A. P. (2009). Saturn atmospheric structure and dynamics. In M.K. Dougherty, L.W. Esposito, & S.M. Krimigis (Eds.), *Saturn from Cassini-Huygens* (pp. 113–159). Dordrecht, Netherlands: Springer. Retrieved from https://link.springer.com/chapter/10.1007%2F978-1-4020-9217-6_6
- Fletcher, L. N., Irwin, P. G. J., Achterberg, R. K., Orton, G. S., & Flasar, F. M. (2016). Seasonal variability of Saturn's tropospheric temperatures, winds, and para-H₂ from Cassini far-IR spectroscopy. *Icarus*, *264*, 137–159. <https://doi.org/10.1016/j.icarus.2015.09.009>
- Flierl, G. R., Malanotte-Rizzoli, P., & Zabusky, N. J. (1987). Nonlinear waves and coherent vortex structures in barotropic β -plane jets. *Journal of Physical Oceanography*, *17*(9), 1408–1438. [https://doi.org/10.1175/1520-0485\(1987\)017<1408%3ANWACVS>2.0.CO;3B2](https://doi.org/10.1175/1520-0485(1987)017<1408%3ANWACVS>2.0.CO;3B2)
- Gaddis, L., Anderson, J., Becker, K., Becker, T., Cook, D., Edwards, K., et al. (1997). An overview of the Integrated Software for Imaging Spectrometers (ISIS). In *28th Annual Lunar and Planetary Science Conference* (p. 387). Houston, TX. Retrieved from <http://adsabs.harvard.edu/abs/1997LPI....28..387G>
- Godfrey, D. A., & Moore, V. (1986). The saturnian ribbon feature: A baroclinically unstable model. *Icarus*, *68*(2), 313–343. [https://doi.org/10.1016/0019-1035\(86\)90026-6](https://doi.org/10.1016/0019-1035(86)90026-6)
- Keszthelyi, L., Becker, T. L., Sides, S., Barrett, J., Cook, D., Lambright, S., et al. (2013). Support and future vision for the integrated software for imagers and spectrometers (ISIS). In *Paper presented at 44th Lunar and Planetary Science Conference* (p. 2546). The Woodlands, TX. Retrieved from <http://adsabs.harvard.edu/abs/2013LPI....44.2546K>
- Lindal, G. F., Sweetnam, D. N., & Eshleman, V. R. (1985). The atmosphere of Saturn: An analysis of the Voyager radio occultation measurements. *The Astronomical Journal*, *90*, 1136–1146. <http://adsabs.harvard.edu/abs/1985AJ....90.1136L>
- Markwardt, C. B. (2009). Non-linear least squares fitting in IDL with MPFIT. In D. A. Bohlender, D. Durand, & P. Dowler (Eds.), *Astronomical data analysis software and systems XVIII* (p. 251). San Francisco, CA: Astronomical Society of the Pacific. Retrieved from <http://adsabs.harvard.edu/abs/2009ASPC..411..251M>
- Morales-Juberías, R., Sayanagi, K. M., Simon, A. A., Fletcher, L. N., & Cosentino, R. G. (2015). Meandering shallow atmospheric jet as a model of Saturn's north-polar hexagon. *The Astrophysical Journal Letters*, *806*(1), L18. <https://doi.org/10.1088/2041-8205/806/1/L18>
- Pedlosky, J. (2003). *Waves in the ocean and atmosphere: Introduction to wave dynamics*. Berlin: Springer. <https://doi.org/10.1007/978-3-662-05131-3>
- Porco, C. C., West, R. A., Squyres, S., McEwen, A., Thomas, P., Murray, C. D., et al. (2004). Cassini imaging science: Instrument characteristics and anticipated scientific investigations at Saturn. *Space Science Reviews*, *115*(1-4), 386–497. <https://doi.org/10.1007/s11214-004-1456-7>
- Poulin, F. J., & Flierl, G. R. (2003). The nonlinear evolution of barotropically unstable jets. *Journal of Physical Oceanography*, *33*(10), 2173–2192. [https://doi.org/10.1175/1520-0485\(2003\)033<2173:TNEOBU>2.0.CO;2](https://doi.org/10.1175/1520-0485(2003)033<2173:TNEOBU>2.0.CO;2)
- Read, P. L., Conrath, B. J., Fletcher, L. N., Gierasch, P. J., Simon-Miller, A. A., & Zuchowski, L. C. (2009). Mapping potential vorticity dynamics on Saturn: Zonal mean circulation from Cassini and Voyager data. *Planetary and Space Science*, *57*(14-15), 1682–1698. <https://doi.org/10.1016/j.pss.2009.03.004>
- Rogers, J. H., Fletcher, L. N., Adamoli, G., Jacquesson, M., Vedovato, M., & Orton, G. S. (2016). A dispersive wave pattern on Jupiter's fastest retrograde jet at 20° S. *Icarus*, *277*, 354–369. <https://doi.org/10.1016/j.icarus.2016.05.028>
- Roman, M. T., Banfield, D., & Gierasch, P. J. (2013). Saturn's cloud structure inferred from Cassini ISS. *Icarus*, *225*(1), 93–110. <https://doi.org/10.1016/j.icarus.2013.03.015>
- Sánchez-Lavega, A. (2002). Observations of Saturn's ribbon wave 14 years after its discovery. *Icarus*, *158*(1), 272–275. <https://doi.org/10.1006/icar.2002.6864>
- Sánchez-Lavega, A. (2011). *An introduction to planetary atmospheres*. Boca Raton, FL: CRC Press. <https://doi.org/10.1201/9781439894668>
- Sánchez-Lavega, A., del Río-Gaztelurrutia, T., Delcroix, M., Legarreta, J. J., Gómez-Forrellad, J. M., Hueso, R., et al. (2012). Ground-based observations of the long-term evolution and death of Saturn's 2010 great white spot. *Icarus*, *220*(2), 561–576. <https://doi.org/10.1016/j.icarus.2012.05.033>
- Sánchez-Lavega, A., del Río-Gaztelurrutia, T., Hueso, R., Pérez-Hoyos, S., García-Melendo, E., Antuñaño, A., et al. (2014). The long-term steady motion of Saturn's hexagon and the stability of its enclosed jet stream under seasonal changes. *Geophysical Research Letters*, *41*, 1425–1431. <https://doi.org/10.1002/2013GL059078>
- Sánchez-Lavega, A., Rojas, J. F., & Sada, P. V. (2000). Saturn's zonal winds at cloud level. *Icarus*, *147*(2), 405–420. <https://doi.org/10.1006/icar.2000.6449>
- Sayanagi, K. M., Dyudina, U. A., Ewald, S. P., Fischer, G., Ingersoll, A. P., Kurth, W. S., et al. (2013). Dynamics of Saturn's great storm of 2010-2011 from Cassini ISS and RPWS. *Icarus*, *223*(1), 460–478. <https://doi.org/10.1016/j.icarus.2012.12.013>
- Sayanagi, K. M., Morales-Juberías, R., & Ingersoll, A. P. (2010). Saturn's northern hemisphere ribbon: Simulations and comparison with the meandering Gulf Stream. *Journal of the Atmospheric Sciences*, *67*(8), 2658–2678. <https://doi.org/10.1175/2010JAS3315.1>
- Seidelmann, P. K., Archinal, B. A., A'Hearn, M. F., Conrad, A., Consolmagno, G. J., Hestroffer, D., et al. (2007). Report of the IAU/IAG working group on cartographic coordinates and rotational elements: 2006. *Celestial Mechanics and Dynamical Astronomy*, *98*(3), 155–180. <https://doi.org/10.1007/s10569-007-9072-y>
- Smith, B. A., Soderblom, L., Batson, R., Bridges, P., Inge, J., Masursky, H., et al. (1982). A new look at the Saturn system: The Voyager 2 images. *Science*, *215*, 504–537. <https://doi.org/10.1126/science.215.4532.504>

- Smith, B. A., Soderblom, L., Beebe, R., Boyce, J., Briggs, G., Bunker, A., et al. (1981). Encounter with Saturn: Voyager 1 imaging science results. *Science*, 212, 163–191. <https://doi.org/10.1126/science.212.4491.163>
- Sromovsky, L. A., Baines, K. H., Fry, P. M., & Momary, T. W. (2016). Cloud clearing in the wake of Saturn's Great Storm of 2010-2011 and suggested new constraints on Saturn's He/H₂ ratio. *Icarus*, 276, 141–162. <https://doi.org/10.1016/j.icarus.2016.04.031>
- Sromovsky, L. A., Revercomb, H. E., Krauss, R. J., & Suomi, V. E. (1983). Voyager 2 observations of Saturn's northern mid-latitude cloud features: Morphology, motions, and evolution. *Journal of Geophysical Research*, 88(A11), 8650–8666. <https://doi.org/10.1029/JA088iA11p08650>
- Tange, O. (2011). GNU parallel—the command-line power tool. *The USENIX Magazine*, 36(1), 42–47.
- Vasavada, A. R., Hörst, S. M., Kennedy, M. R., Ingersoll, A. P., Porco, C. C., Del Genio, A. D., & West, R. A. (2006). Cassini imaging of Saturn: Southern hemisphere winds and vortices. *Journal of Geophysical Research*, 111, E05004. <https://doi.org/10.1029/2005JE002563>
- West, R., Knowles, B., Birath, E., Charnoz, S., Di Nino, D., Hedman, M., et al. (2010). In-flight calibration of the Cassini imaging science sub-system cameras. *Planetary and Space Science*, 58(11), 1475–1488. <https://doi.org/10.1016/j.pss.2010.07.006>